



Article

# MoSe<sub>2</sub>-WS<sub>2</sub> Nanostructure for an Efficient Hydrogen Generation under White Light LED Irradiation

Tatiparti Padma <sup>1,†</sup>, Dheeraj Kumar Gara <sup>2</sup> , Amara Nadha Reddy <sup>2</sup>, Surya Veerendra Prabhakar Vattikuti <sup>3,†</sup>  and Christian M. Julien <sup>4,\*</sup> 

<sup>1</sup> Department of Electronics & Communications Engineering, Gokaraju Rangaraju Institute of Engineering and Technology, Kukatpally, Hyderabad 500090, Telangana, India; propadmat@gmail.com

<sup>2</sup> Malla Reddy College of Engineering and Technology, Doolapally, Hyderabad 500100, Telangana, India; dheeru498@gmail.com (D.K.G.); amarnadha@gmail.com (A.N.R.)

<sup>3</sup> School of Mechanical Engineering, Yeungnam University, Gyeongsan 38541, Korea; vsvprabu@gmail.com

<sup>4</sup> Institut de Minéralogie, de Physique des Matériaux et de Cosmochimie (IMPMC), Sorbonne Université, CNRS-UMR 7590, 4 Place Jussieu, 75252 Paris, France

\* Correspondence: christian.julien@sorbonne-universite.fr

† These authors contributed equally to this work.

**Abstract:** In this work, MoSe<sub>2</sub>-WS<sub>2</sub> nanocomposites consisting of WS<sub>2</sub> nanoparticles covered with few MoSe<sub>2</sub> nanosheets were successfully developed via an easy hydrothermal synthesis method. Their nanostructure and photocatalytic hydrogen evolution (PHE) performance are investigated by a series of characterization techniques. The PHE rate of MoSe<sub>2</sub>-WS<sub>2</sub> is evaluated under the white light LED irradiation. Under LED illumination, the highest PHE of MoSe<sub>2</sub>-WS<sub>2</sub> nanocomposite is 1600.2 μmol g<sup>-1</sup> h<sup>-1</sup>. When compared with pristine WS<sub>2</sub>, the MoSe<sub>2</sub>-WS<sub>2</sub> nanostructures demonstrated improved PHE rate, which is 10-fold higher than that of the pristine one. This work suggests that MoSe<sub>2</sub>-WS<sub>2</sub> could be a promising photocatalyst candidate and might stimulate the further studies of other layered materials for energy conversion and storage.

**Keywords:** hydrogen production; layered materials; photocatalysts; WS<sub>2</sub>; MoSe<sub>2</sub>



**Citation:** Padma, T.; Gara, D.K.; Reddy, A.N.; Vattikuti, S.V.P.; Julien, C.M. MoSe<sub>2</sub>-WS<sub>2</sub> Nanostructure for an Efficient Hydrogen Generation under White Light LED Irradiation. *Nanomaterials* **2022**, *12*, 1160. <https://doi.org/10.3390/nano12071160>

Received: 22 February 2022

Accepted: 30 March 2022

Published: 31 March 2022

**Publisher's Note:** MDPI stays neutral with regard to jurisdictional claims in published maps and institutional affiliations.



**Copyright:** © 2022 by the authors. Licensee MDPI, Basel, Switzerland. This article is an open access article distributed under the terms and conditions of the Creative Commons Attribution (CC BY) license (<https://creativecommons.org/licenses/by/4.0/>).

## 1. Introduction

Presently, energy shortage and environmental pollution are the major problems [1–3]. Intuitively, the current photocatalytic hydrogen (H<sub>2</sub>) generation from water through semiconductor nanostructures is an ideal approach, and this technique is considered as a potential, economical way to overcome the issue of energy shortage [4–7]. Over the years, there has been substantial experimental data calibrated on transition-metal (TM) oxide-based photocatalysts for energy-storage applications [6–8] with minimal environmental pollution. Though these materials display excellent photocatalytic activity just beneath the UV illumination, they exhibit poor activity in visible light due to their wide bandgap. In order to stimulate photocatalytic activity in visible light, recent attempts on anion-doped TM oxides-, sulfides-, and selenides-based nanostructures have been reported [9,10]. However, these TMs are unstable, making them inert towards commercial applications. Henceforth, there is a challenge for the researchers to identify and develop potential, stable and economically novel photocatalysts for H<sub>2</sub> evolution.

In lieu of this, the two-dimensional (2D) MoSe<sub>2</sub> semiconductor is a compelling potential catalyst for next-generation hydrogen evolution due to its narrow bandgap (1.2 eV), specific surface area and more metallic nature, which prompts higher electrical conductivity that is more favorable to hydrogen evolution reactions. However, there are few reports on the preparation of MoSe<sub>2</sub>-based composites through diverse approaches, which display an enhanced photocatalytic activity (PCA) when compared with the bare MoSe<sub>2</sub> [11]. In spite of this enhanced photocatalyst, there is provision to promote further the PCA in the

water-splitting process by resolving the photo corrosion and faster charge recombination problems. In this context, an inclination towards the development of a nanostructure heterojunction, which can improve the visible light absorption, further altering the surface defects followed by reduction in the surface recombination. This may enhance the capability of water splitting both quantitatively and qualitatively. Recently, 2D-layered WS<sub>2</sub> has enticed significant attention in the field of energy and photocatalysis applications because of its promising characteristics towards photocatalytic performance [11,12]. There is a decent work available in the scientific literature on WS<sub>2</sub>-based composites, which displayed significant enhancement in the PCA compared to pristine WS<sub>2</sub> [12–14]. Various methods have been reported in the literature to process these composites [15,16]. However, in addition to this, the interest of an advanced study combining two transition-metal dichalcogenides (TMDs) such as MoSe<sub>2</sub> and WS<sub>2</sub> possessing alike hexagonal structure, enables to simulation of the heterojunction formation.

The MoX<sub>2</sub>/WX<sub>2</sub> (X = S, Se) heterostructures, which exhibit a type-II band configuration, are considered to be efficient systems for the production of optoelectronic and photovoltaic devices, in which the free electrons and holes are spontaneously isolated [17]. The lattice constants of MoX<sub>2</sub> and WX<sub>2</sub> being very close to each other indicate that MoX<sub>2</sub>-WX<sub>2</sub> heterostructures can have minimum structural defects. According to the theoretical calculations, the conduction band minimum (CBM) of the WS<sub>2</sub> is only slightly lower than that of the MoSe<sub>2</sub> [18]. In 2018, Jin et al. reviewed experimental and theoretical efforts to elucidate electron dynamics in TMDC heterostructures [19]. The dominant interlayer electron transport relaxation pathway in WS<sub>2</sub>/MoSe<sub>2</sub> heterostructures proving the strong interlayer dipole–dipole interaction was identified by Kozawa et al. [20]. Photoluminescence excitation spectroscopy evidenced the fast interlayer energy transfer across the van der Waals interface of the MoSe<sub>2</sub>/WS<sub>2</sub> heterostructures. Meng et al. investigated the ultrafast carrier transfer, which can efficiently separate electrons and holes in the intralayer excitons in a MoSe<sub>2</sub>/WS<sub>2</sub> heterostructure [21]. Based on first-principles ab initio calculations, Amin et al. investigated the band structure of WS<sub>2</sub>/MoSe<sub>2</sub> and showed the indirect electron transition semiconducting behavior [17]. The distinctive interactions between stacked layer are essential for solar cells because the confinement of electrons by MoSe<sub>2</sub> and holes by WS<sub>2</sub>, leading to a spontaneous charge separation when excitons scatter to the WS<sub>2</sub>/MoSe<sub>2</sub> junction [22]. Ceballos et al. evidenced highly efficient and anomalous charge transfer in the van der Waals MoSe<sub>2</sub>/WS<sub>2</sub>/MoS<sub>2</sub> trilayer semiconductors [23]. Wu et al. fabricated a WS<sub>2</sub>/MoSe<sub>2</sub> hybrid semiconductor catalyst (WS<sub>2</sub> mass fraction of 20%) with a p-n heterojunction, which is composed of spherical WS<sub>2</sub> particles (2 μm diameter) mixed with flower-like granular MoSe<sub>2</sub> (50 nm in size). This product exhibits good photocatalytic performance with a photocurrent density of 35 μA cm<sup>-2</sup> at -0.6 V vs. SCE [24].

Moreover, experimental and theoretical investigations have shown that the unsaturated X-edges of TMDs are favorable to hydrogen evolution electrocatalytic activity [25]. Band offsets and heterostructures of monolayer and few-layer TMDs were calculated using the vacuum level as reference, and a simple model was proposed to explain the observed chemical trends [26]. This concept has been applied to the MoS<sub>2</sub>/WS<sub>2</sub> and MoS<sub>2</sub>/WSe<sub>2</sub> heterostructures, which exhibited robust electrocatalytic properties [27]. Recently, Vikraman et al. have constructed a MoSe<sub>2</sub>/WS<sub>2</sub> heterojunction model by a chemical/physical process and have intricately examined its hydrogen evolution reaction performances [28]. The MoSe<sub>2</sub>/WS<sub>2</sub> heterostructure displayed excellent electrocatalytic hydrogen evolution behavior with a 75 mV overpotential to drive a 10 mA·cm<sup>-2</sup> current density, a 60 mV·dec<sup>-1</sup>. Such a type of structure is developed as an active electrode for hydrogen evolution to replace the nonabundant Pt.

To the best of our knowledge, both photocatalytic hydrogen evolution (PHE) and electrocatalytic hydrogen evolution (EHE) performance of the van der Waals two-layer MoSe<sub>2</sub>-WS<sub>2</sub> heterostructure has not been studied yet. Only a mixture of WS<sub>2</sub> and MoSe<sub>2</sub> particles was considered. The main goal of the present work was to synthesize a MoSe<sub>2</sub>-WS<sub>2</sub> nanocomposite through hydrothermal process and further elucidate its photocatalytic

and electrocatalytic properties for hydrogen evolution. As anticipated, the MoSe<sub>2</sub>-WS<sub>2</sub> nanostructure displayed better PHE rate than that of pristine WS<sub>2</sub> sample. It is demonstrated that the PHE of MoSe<sub>2</sub>-WS<sub>2</sub> is 10-fold higher than that of WS<sub>2</sub>.

## 2. Materials and Methods

The raw materials sodium tungstate dehydrates, polyethylene glycol, and thioacetamide were purchased from Sigma-Aldrich (St. Louis, MO, USA). Ammonium molybdate tetrahydrate was from Junsei Chemical Co. (Tokyo, Japan). Polyvinylpyrrolidone (PVP), Selenium powder and anhydrous oxalic acid were provided from Daejung (Daejeon, Korea) and used as received without further treatment.

### 2.1. Preparation of WS<sub>2</sub>

The synthesis procedure for WS<sub>2</sub> followed that of Yuan et al. [29] with modification. Typically, 1.1 g of sodium tungstate dehydrate, 2.3 g of thioacetamide, and 5.5 mL of polyethylene glycol were dissolved in 25 mL of deionized water followed by stirring to obtain a homogeneous solution. Then, the pH of the solution was adjusted to 2 by adding the oxalic acid and transferred to sealed autoclave-reactor solution that was maintained at 210 °C for 48 h. After cooling, the precipitates were collected by centrifuge at 9000 rpm, washed with water and ethanol for several times, and dried in a vacuum oven for 100 °C for 48 h and then annealed at 600 °C for 1 h under Ar to obtain the final product.

### 2.2. Preparation of MoSe<sub>2</sub>-WS<sub>2</sub>

Typically, 0.025 mol of NH<sub>4</sub>Mo<sub>7</sub>O<sub>24</sub>·4H<sub>2</sub>O and 0.12 g of PVP were dissolved in 12 mL of ammonium hydroxide solution under constant stirring. On the other hand, 0.05 mol of Se powder was dispersed in hydrazine hydrate under vigorous stirring for 30 min. Then, this solution was added dropwise to the above resultant solution at room temperature, which has a nominal Mo/Se molar ratio of 1:2. After that, 25 mg of WS<sub>2</sub> was added into resultant solution stirred for about 1 h. The resulting homogenous solution was irradiated by hydrothermal reaction at 220 °C for 48 h. The as-obtained precipitate (MoSe<sub>2</sub>-WS<sub>2</sub>) was collected by centrifugation at 9000 rpm, washed with a mixture of deionized water and ethanol, and dried in a vacuum oven at 130 °C for 48 h. To make a comparison, pure MoSe<sub>2</sub> was also synthesized from the similar procedure without WS<sub>2</sub>.

### 2.3. Instruments

X-ray diffraction (XRD) patterns were analyzed on Shimadzu 6100 X-ray diffractometer (Shimadzu Corp., Tokyo, Japan) equipped with a CuK<sub>α</sub> X-ray source ( $\lambda = 1.5406 \text{ \AA}$ ). The morphology analysis was performed by transmission electron microscopy (TEM), high-resolution TEM (HRTEM) and high-angle annular dark field-scanning transmission electron microscopy (HAADF-STEM) using a FEI Tecnai G2 F20 (FEI Company, Hillsboro, OR, USA). Initially, the synthesized MoSe<sub>2</sub>-WS<sub>2</sub> nanocomposites were dispersed in ethanol and sonicated for 10 min, then the dispersed MoSe<sub>2</sub>-WS<sub>2</sub> was dropped on a TEM grid (200 mesh Cu grid) and dried at 90 °C overnight.

The X-ray photoelectron spectra (XPS) were recorded using a Thermo Scientific k- $\alpha$  surface analyzer (ThermoFisher Scientific, Alachua, FL, USA), equipped with a AlK<sub>α</sub> X-ray source ( $h\nu = 1486 \text{ eV}$ ). The ultraviolet–visible (UV-Vis) spectroscopy was carried out on a Cary 5000 (ThermoFisher Scientific, Alachua, FL, USA) in the 200–800 nm wavelength range using a transmittance and reflectance equipment. The infrared spectra were recorded in the spectral range of 400–4000 cm<sup>-1</sup> using an Avatar 370 Fourier transform infrared spectrometer (FTIR, Thermo Nicolet, Alachua, FL, USA). The Brunauer-Emmett-Teller (BET) method was used to determine the specific surface area and pore size distribution measured by an ASAP 2420 surface area analyzer degassed for 1 h at 150 °C (Micromeritics, Norcross, GA, USA). High-resolution transmission electron microscope (HRTEM Titan G2 Chemi STEM Cs probe, FEI Company, Hillsboro, OR, USA) with EDS windowless (Super-X

model) and physisorption analyzer (BET-Micromeritics, 3FLEX, Norcross, GA, USA) were used for both morphology and surface area studies.

#### 2.4. Photocatalytic Hydrogen Tests

The photoreaction was conducted in a quartz top-irradiation reactor tightened with silicone rubber “Septa”. Then, 5 mg of photocatalysts and 5 mL of Na<sub>2</sub>S/Na<sub>2</sub>SO<sub>3</sub> were dispersed into 45 mL of water by sonication for 40 min. The reactor was evacuated for 45 min and N<sub>2</sub>-bubbled for 30 min prior to irradiation. A light-emitting diode (LED, white light irradiation) was facilitated by 100 W lamp without an optical filter. The induced gases were measured using a gas chromatograph (YL-6500 with TCD detector) equipped with a 5-Å molecular sieve column under He carrier gas.

#### 2.5. Electrochemical Measurements

Electrochemical characterizations were performed with a Bio-Logic (SP-200) workstation with a standard three-electrode cell using Ag/AgCl (3.5 mol L<sup>-1</sup> KCl solution), a platinum coil and fluorine-doped tin oxide (FTO) glass as reference, counter and working electrodes, respectively. The working electrode was prepared as follows: 5 mg of catalysts and 80 µL of 5 wt.% Nafion solution were dispersed in 1 mL of a solution of deionized water and ethanol, i.e., 4:1 in volume ratio, and then stirred for 45 min. A total of 5 µL of the resultant solution was drop-casted on the FTO glass. The working electrode was dried at 75 °C for 1 h. Photocurrent measurements and electrochemical impedance spectroscopy analyses were carried out in 0.5 mol L<sup>-1</sup> Na<sub>2</sub>SO<sub>4</sub> solution with purging nitrogen gas.

### 3. Results and Discussion

#### 3.1. XRD Analysis

The phase purity and crystal structure of the as-prepared nanostructures were analyzed through bulk X-ray diffraction. Figure 1 displays the XRD patterns of WS<sub>2</sub>, MoSe<sub>2</sub> pristine materials and that of the MoSe<sub>2</sub>-WS<sub>2</sub> nanocomposite in the 2θ range 10–80°. The diffraction peaks at 13.7°, 28.21°, 34.11°, 39.49°, and 58.89° corresponding to the (002), (004), (100), (103), and (008) crystal planes, respectively, match well with the hexagonal structure of WS<sub>2</sub> (JCPDS Card # 08-0237) [29–31].

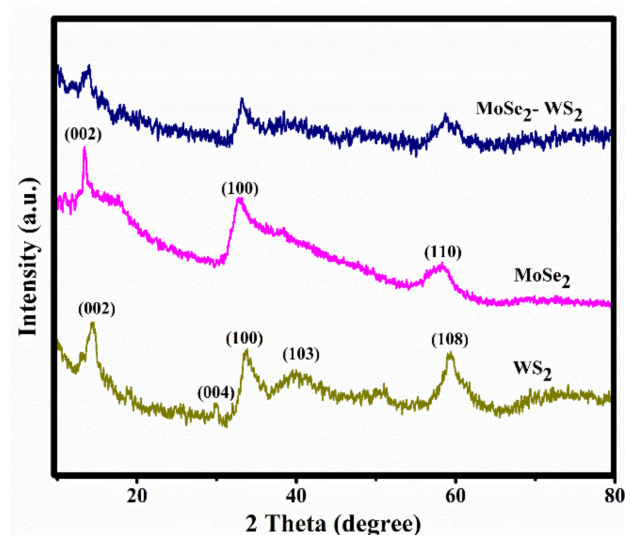


**Figure 1.** XRD patterns of pristine WS<sub>2</sub> and MoSe<sub>2</sub>, and nanostructured MoSe<sub>2</sub>-WS<sub>2</sub> composite. Spectra were recorded using a CuK<sub>α</sub> X-ray source ( $\lambda = 1.5406 \text{ \AA}$ ).

The as-synthesized MoSe<sub>2</sub> similarly displays a hexagonal structure and XRD patterns are in good agreement with literature data (JCPDS Card # 29-0914) [32]. No other impurity peaks were detected. The peak positions of the as-prepared MoSe<sub>2</sub>-WS<sub>2</sub> sample are identical



to those of  $WS_2$  showing that layered  $MoSe_2$  does not substitute into the  $WS_2$  lattice. Although, an obvious decrease in the peak intensity is noticed, while no peaks related to  $MoSe_2$  are recognized due to its good dispersion and its low loading content.

### 3.2. Morphology and Elemental Analysis

HRTEM was employed to probe the morphology of the as-synthesized  $MoSe_2$ - $WS_2$  nanocomposite (Figure 2a–d). As depicted, the typical sheet-like structure of  $MoSe_2$  can be distinctly noticed. Some  $MoSe_2$  slabs with the characteristic layered structure are remarkable on the surface of  $WS_2$  particles (see Figure 2b–d). In addition, the HAADF-STEM elemental mapping images shown in Figure 2e–i clearly depict that W (yellow), Mo (purple), S (dark blue), and Se (light blue) are uniformly distributed on the surface of nanostructures. These findings indicate that the  $MoSe_2$ - $WS_2$  nanocomposite heterostructures were effectively prepared.

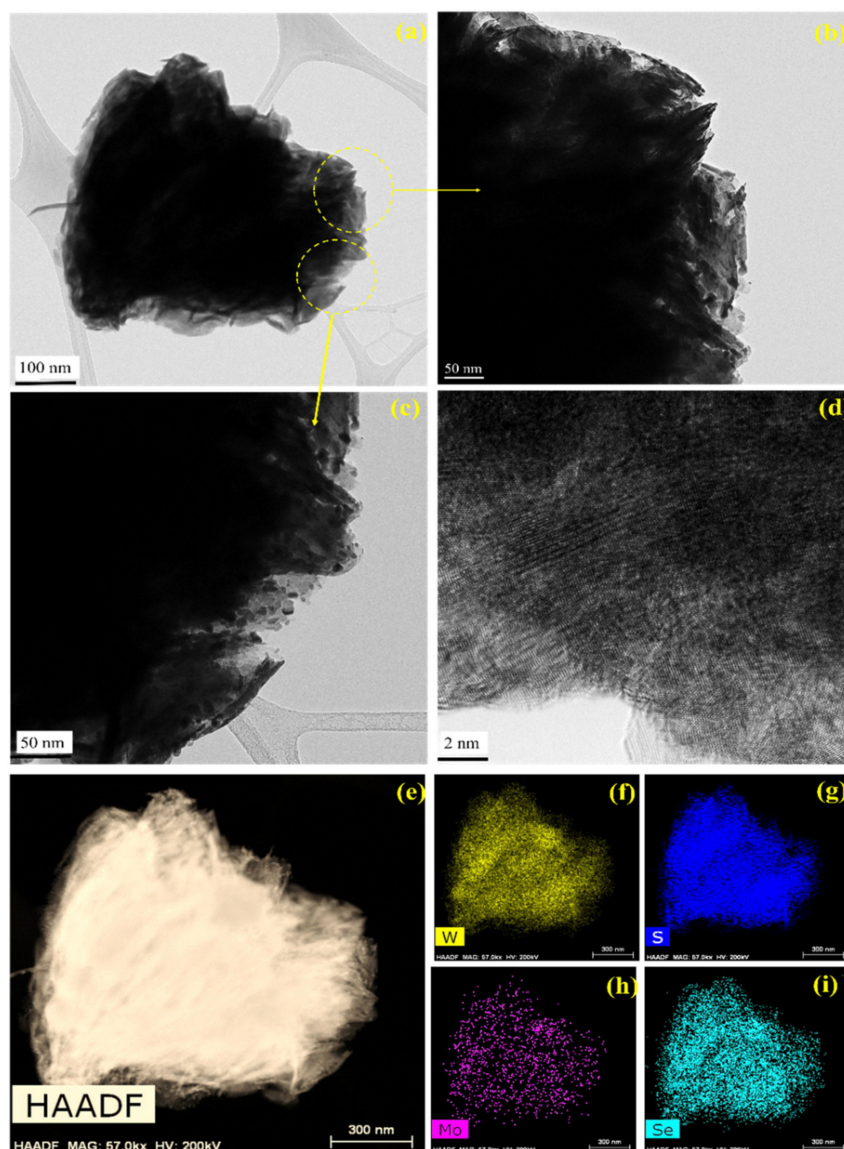


**Figure 2.** (a–c) TEM images of the  $MoSe_2$ - $WS_2$  nanocomposite, (d) HRTEM image, (e) HAADF-STEM pattern, and (f–i) corresponding elemental mapping images of W, S, Mo and Se.

### 3.3. XPS Analysis

Figure 3 presents the XPS magnified scans of (a) W, (b) Mo, (c) S and (d) Se of the  $MoSe_2$ - $WS_2$  sample and confirms the existence of  $MoSe_2$  and  $WS_2$ . Figure 3a depicts the W

4f peaks at binding energies of 32.1, 34.1, 36.2, and 28.3 eV corresponding to the  $W^{4+} 4f_{7/2}$ ,  $W^{4+} 4f_{5/2}$ ,  $W^{6+} 4f_{7/2}$ , and  $W^{6+} 4f_{5/2}$  core level, respectively, which indicates the existence of  $W^{4+}$ ,  $W^{6+}$  species in the synthesized  $MoSe_2$ - $WS_2$  [31]. The higher binding energy of 36.2 eV signifies the existence of the +6 oxidation state of W element, with a very low peak intensity specifying that only a small portion of  $W^{4+}$  cations is oxidized when the sample is in contact with the air [32]. Figure 3b shows the Mo 3d contribution with peaks located at 228.0 and 232.6 eV, belonging to the  $Mo^{4+} 3d_{5/2}$  and  $Mo^{4+} 3d_{3/2}$  core level of  $MoSe_2$ . The valence states of the Mo element corresponding to the double peaks at 231.2 and 235.1 eV are assigned to  $Mo^{6+} 3d_{5/2}$  and  $Mo^{6+} 3d_{3/2}$  core levels specifying the oxidized states of Mo due to air contact [16,17]. The S 2p peak can be deconvoluted into two peaks at 163.6 and 161.8 eV (Figure 3c) corresponding to the S  $2p_{1/2}$  and S  $2p_{3/2}$  core levels with doublet positioned at 166.98 and 160.97 eV, which can be attributed to the Se  $3p_{1/2}$  and Se  $3p_{1/2}$  core levels [33]. Finally, Figure 3d displays the binding energies of Se  $3d_{5/2}$  at 54.3 eV and Se  $3d_{3/2}$  at 55.2 eV, corresponding to the divalent ( $-2$ ) state of Se. All these values match well with those reported in previous investigations and indicate the anticipated chemical states of  $Mo^{4+}$ ,  $W^{4+}$ ,  $Se^{2-}$ , and  $S^{2-}$  in the  $MoSe_2$ - $WS_2$  nanostructure [31].

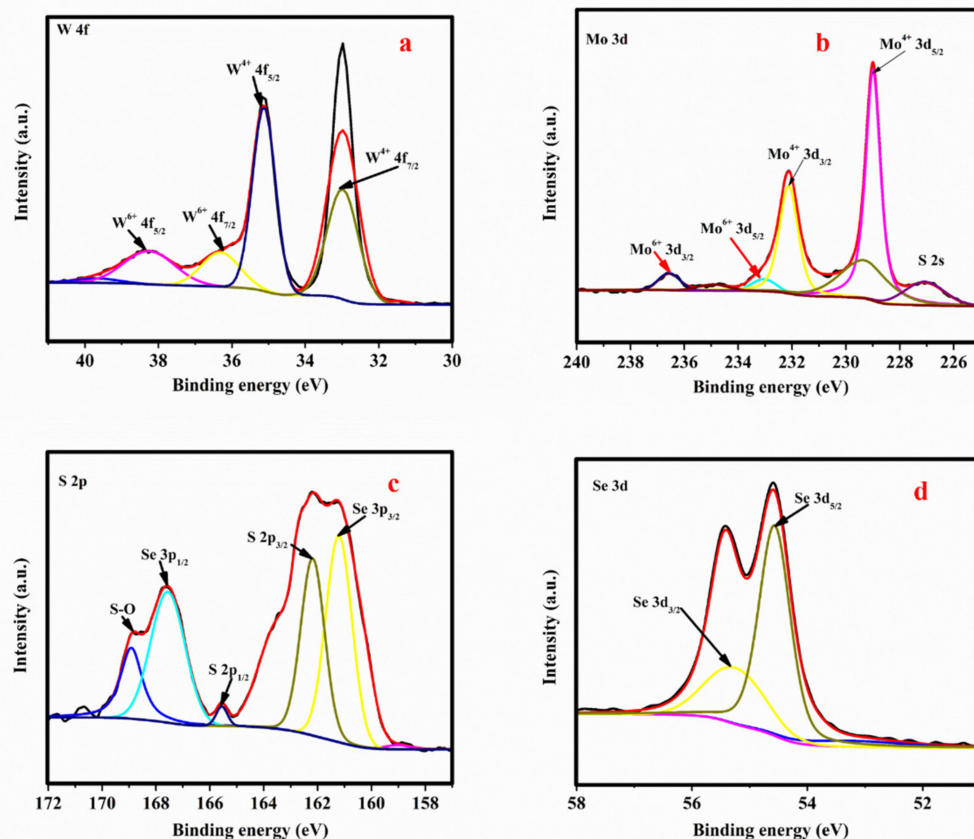


**Figure 3.** XPS elemental profiles of (a) W, (b) Mo, (c) S, and (d) Se elements of the  $MoSe_2$ - $WS_2$  nanostructure.

### 3.4. FTIR Analysis

Figure 4 shows the FTIR spectra of  $WS_2$ ,  $MoSe_2$  and  $MoSe_2$ - $WS_2$  samples recorded in the range  $400$ – $4000\text{ cm}^{-1}$ . In the FTIR spectrum of  $WS_2$ , the bands pointed at  $743$ ,  $1739$  and  $2943\text{ cm}^{-1}$  are attributed to the W-S bending and stretching vibrations, and hydroxyl groups related to O-H bonds, respectively [33,34]. In the  $MoSe_2$  spectrum, the bands located at  $523$ ,  $1218$ ,  $1327$ ,  $1744$  and  $3013\text{ cm}^{-1}$  could be ascribed to the stretching vibration of Mo-Se and hydroxyl groups of  $MoSe_2$  [35]. For the  $MoSe_2$ - $WS_2$ , the band intensities corresponding to the hydroxyl group decrease significantly, and the infrared band of the

Se-W-S bonds shifts from  $743$  to  $622\text{ cm}^{-1}$ , which suggests the interface interaction between the  $\text{MoSe}_2$  and  $\text{WS}_2$ .

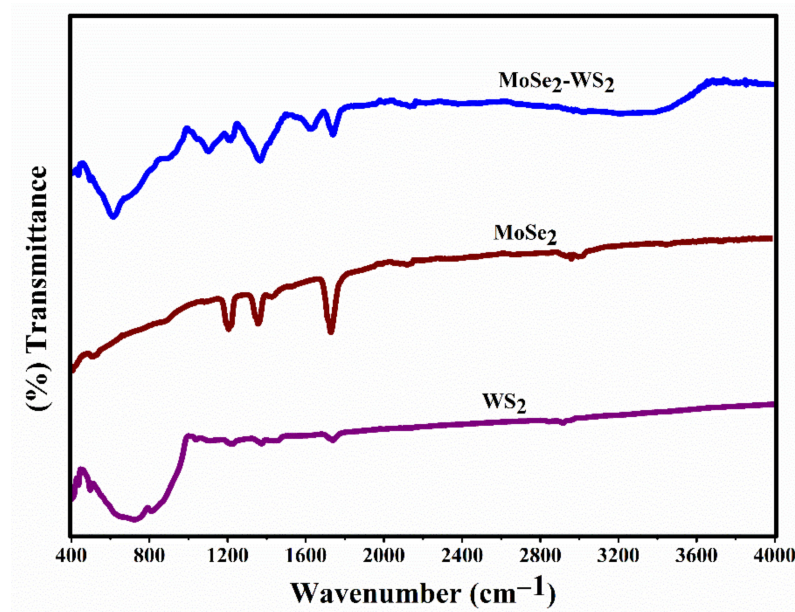


Figure 4. FTIR spectra of  $\text{WS}_2$ ,  $\text{MoSe}_2$ , and  $\text{MoSe}_2\text{-WS}_2$  catalysts.

### 3.5. Surface Area Analysis

Figure 5a shows the  $\text{N}_2$  adsorption–desorption isotherms of pristine  $\text{WS}_2$  and  $\text{MoSe}_2\text{-WS}_2$  samples. Both samples show the standard type-IV isotherms with obvious hysteresis loops, endorsing the presence of hierarchical mesoporosity [36]. On the other hand, the sharp uptakes at high pressure  $0.55\text{--}1.0 P/P_0$  of  $\text{WS}_2$  and  $\text{MoSe}_2\text{-WS}_2$  indicate the presence of mesopores in both samples, which is in good agreement with the results of pore size distribution curves as shown in Figure 5b. Data are listed in Table 1. The  $\text{MoSe}_2\text{-WS}_2$  nanocomposite has a high specific surface area of  $132.79\text{ m}^2\text{ g}^{-1}$ , which is slightly higher than pristine  $\text{WS}_2$  ( $106.23\text{ m}^2\text{ g}^{-1}$ ). On the other hand, both samples exhibit almost the same pore size:  $10.6(5)\text{ nm}$  for  $\text{MoSe}_2\text{-WS}_2$  and  $10.7(2)\text{ nm}$  for  $\text{WS}_2$ .

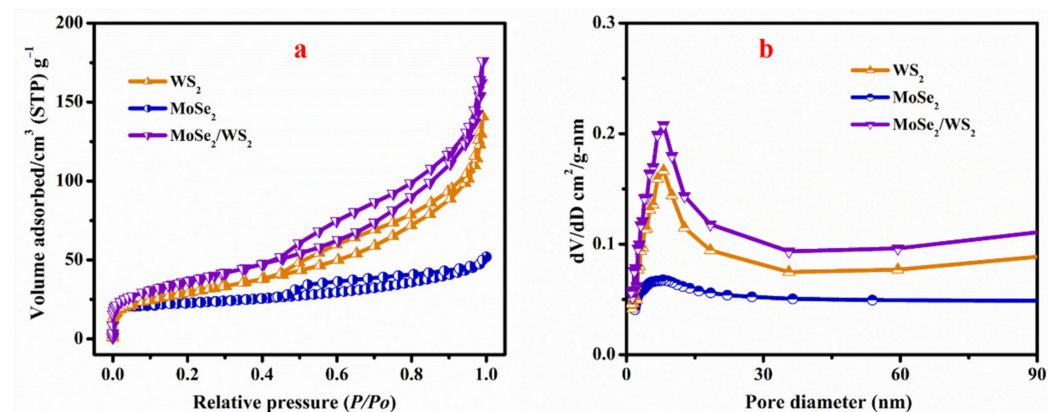


Figure 5. (a) BET profiles and (b) pore distribution of pristine  $\text{WS}_2$ ,  $\text{MoSe}_2$ , and  $\text{MoSe}_2\text{-WS}_2$  samples.



**Table 1.** BET analysis results of pristine WS<sub>2</sub> and MoSe<sub>2</sub>-WS<sub>2</sub> nanostructures.

Sample	BET Surface Area (m <sup>2</sup> g <sup>-1</sup> )	Pore Volume (cm <sup>3</sup> g <sup>-1</sup> )	Pore Size (nm)
WS <sub>2</sub>	106.2	0.214	10.7(2)
MoSe <sub>2</sub>	35.07	0.11	8.3(2)
MoSe <sub>2</sub> -WS <sub>2</sub>	132.8	0.268	10.6(5)

### 3.6. Optical Studies

To evaluate the electronic and optoelectronic properties of the MoSe<sub>2</sub>-WS<sub>2</sub> nanocomposite, the optical bandgap has been determined using the UV-Vis spectroscopy in the vicinity of the fundamental transition, i.e., wavelength range of 200–800 nm, and compared with that of pristine WS<sub>2</sub> and MoSe<sub>2</sub> samples. The UV-Vis transmittance and reflectance spectra of samples are depicted in Figure 6a–f. Analyses of material bandgaps are presented in Figure 6g–i.

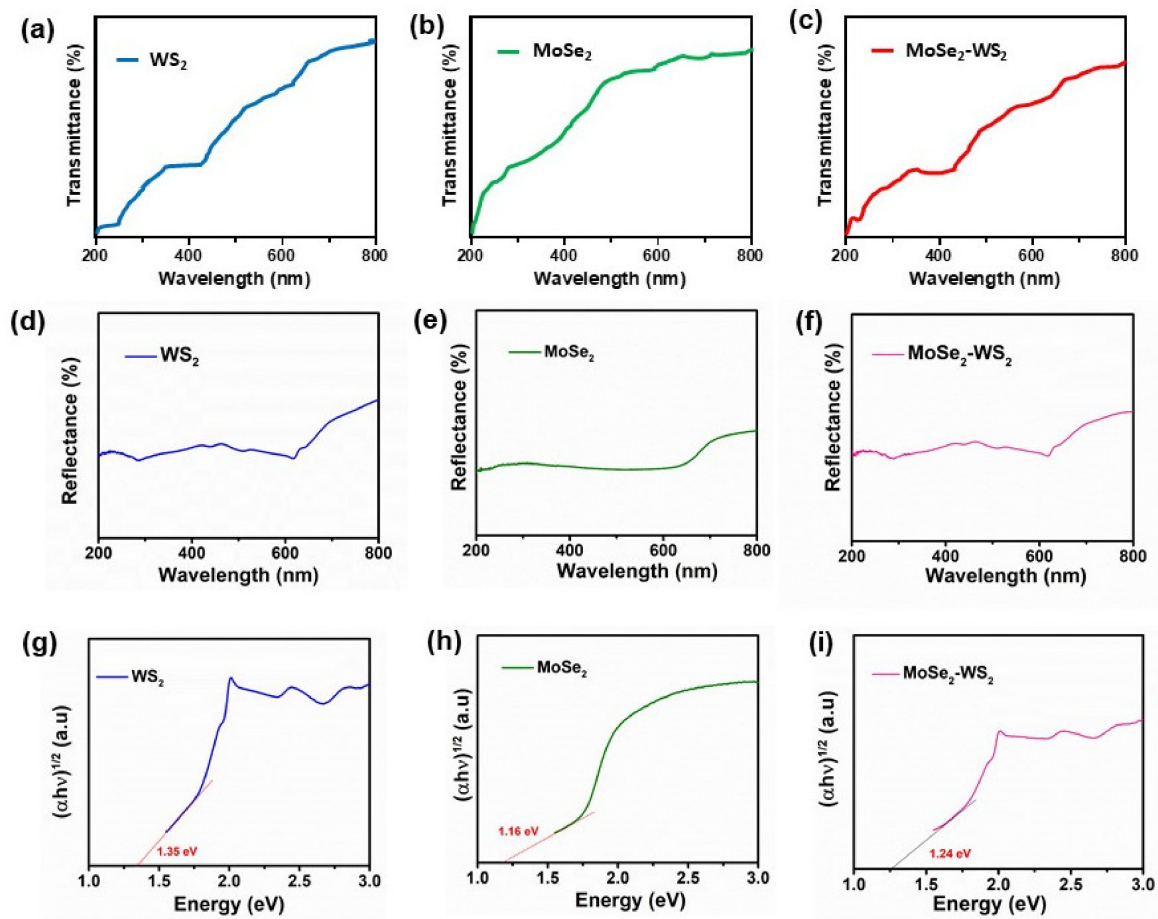


**Figure 6.** Determination of the bandgap of WS<sub>2</sub>, MoSe<sub>2</sub> and MoSe<sub>2</sub>-WS<sub>2</sub> catalysts. (a–c) UV-Vis transmittance spectra, (d–f) UV-Vis reflectance spectra and (g–i) Tauc's plots.

The optical absorption coefficient ( $\alpha$ ) is calculated taking into consideration the transmittance ( $T\%$ ) and reflectance ( $R\%$ ) of the sample using the standard equation [37]:

$$\alpha = \frac{1}{d} \ln \left[ \frac{(1-R)^2}{T} \right], \quad (1)$$



where  $d$  is the film thickness. The bandgap  $E_g$  of samples is calculated by the Tauc's formula [38]:

$$\alpha hv = C (E_g - hv)^n, \quad (2)$$

where  $h$  is the Planck constant,  $\nu$  is the photon energy,  $E_g$  is the average bandgap of the material,  $C$  is a constant depending on several intrinsic properties of the material, i.e., the effective mass of the electron and hole and the material refractive index, and  $n$  is the transition-type dependent. It is equal to 1/2, 3/2, 2 and 3 for the direct-allowed, direct-forbidden, indirect-allowed and indirect-forbidden transitions, respectively [39]. The average bandgap was calculated from the intercept of the linear part of the  $(\alpha hv)^2$  vs.  $hv$  plot on  $x$ -axis for all samples as shown in Figure 6g–i.

The evaluated optical bandgap values ( $\pm 0.02$  eV) are 1.35, 1.16 and 1.24 eV for WS<sub>2</sub>, MoSe<sub>2</sub> and MoSe<sub>2</sub>-WS<sub>2</sub>, respectively. The knowledge of the bandgap is also useful for the phase identification of the samples. It has been demonstrated that 2D TMDs possess sizable bandgaps around 1–2 eV [40]. According to Wang et al. [41], the bandgap of TMDs has the following electronic properties: (i) the bulk has an indirect bandgap of 1.3 eV for WS<sub>2</sub> and 1.1 eV for MoSe<sub>2</sub> and (ii) the monolayer has a direct bandgap of 2.1 eV for WS<sub>2</sub> and 1.5 eV for MoSe<sub>2</sub>. Thus, the bandgap of the MoSe<sub>2</sub>-WS<sub>2</sub> nanocomposite, in which WS<sub>2</sub> is the core of the sample (bulk) and MoSe<sub>2</sub> is formed by few nanosheets covering the bulk is in good agreement with previous reports [36]. Both MoSe<sub>2</sub> and WS<sub>2</sub> layered compounds are expected to undergo a similar indirect-to-direct bandgap evolution with decreasing layer numbers [42]. Indeed, the optical properties of the samples critically depend on the physical properties, and these variations in the energy gap here are consistent with those of the crystallite size.

### 3.7. Photocatalytic Performance

The photocatalytic performances of the as-synthesized products were estimated through water splitting for H<sub>2</sub> evolution. Figure 7a displays the comparison of hydrogen evolution performance of MoSe<sub>2</sub>, WS<sub>2</sub> and MoSe<sub>2</sub>-WS<sub>2</sub> nanostructures for 5 h under LED irradiation. The achieved H<sub>2</sub> production is 600.1, 150.2 and 1600.2  $\mu\text{mol g}^{-1} \text{h}^{-1}$  for MoSe<sub>2</sub>, WS<sub>2</sub>, and MoSe<sub>2</sub>-WS<sub>2</sub>, respectively. The obtained H<sub>2</sub> generation for MoSe<sub>2</sub>-WS<sub>2</sub> is almost 3 and 10 times higher than that of bare MoSe<sub>2</sub> and WS<sub>2</sub>, respectively. It is vital to consider that all the photocatalytic experimental results in this work were employed in an identical condition. The enhanced photocatalytic activity of MoSe<sub>2</sub>-WS<sub>2</sub> nanostructure has the following characteristics: (i) it is due to the formation of heterostructures, which promote the separation of the photocarriers as well as their recombination, (ii) the coupling of MoSe<sub>2</sub> and WS<sub>2</sub> with diverse energy levels could engender the enhancement of the separation and transfer of photoinduced charges, which leads the photoinduced carriers to involve in the photo-redox reactions, and (iii) the MoSe<sub>2</sub> acts as a cocatalyst for generation of H<sub>2</sub>. On the other hand, after a few hours, the volume of the reactor became insufficient to accommodate a large amount of H<sub>2</sub>, which increased solubility of H<sub>2</sub> in the solution, suppressing the production of H<sub>2</sub> in solution, reducing the evolution of H<sub>2</sub> and total scavenger consumption, reducing the ability of H<sub>2</sub> evolution [43]. Thus, it needs to provide additional number of scavengers in the continuous time-on-stream activity of the catalysts. Figure 7b illustrates the continuous stability of MoSe<sub>2</sub>-WS<sub>2</sub> nanostructure over 16 h. After 6 h of continuing H<sub>2</sub> production, it was observed that changing the scavenger and adding scavengers would increase H<sub>2</sub> production, then reduced H<sub>2</sub> production at 11 h and adding the scavenger again at 12 h, the increase in H<sub>2</sub> activity was maintained steadily until 16 h on MoSe<sub>2</sub>-WS<sub>2</sub> nanostructure.

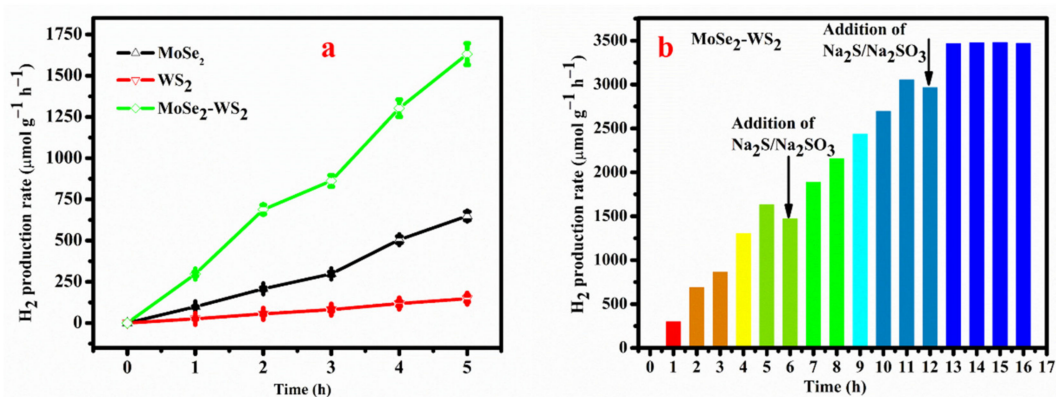


**Figure 7.** (a) H<sub>2</sub> generation rate of MoSe<sub>2</sub>, WS<sub>2</sub>, and MoSe<sub>2</sub>-WS<sub>2</sub> catalysts and (b) continuous cycling stability of MoSe<sub>2</sub>-WS<sub>2</sub> catalyst under visible light irradiation.

These results suggest that the H<sub>2</sub> evolution of the MoSe<sub>2</sub>-WS<sub>2</sub> nanostructure harbors good stability up to three cycles. Therefore, MoSe<sub>2</sub>-WS<sub>2</sub> nanostructures are promising and potential candidates for practical photocatalytic H<sub>2</sub> evolution. Note that the as-prepared MoSe<sub>2</sub>-WS<sub>2</sub> nanocomposite shows better H<sub>2</sub> production yield (10 times greater than that bare WS<sub>2</sub>) than that of the WS<sub>2</sub>-MoS<sub>2</sub> heterostructure (6.5 times greater than that bare WS<sub>2</sub>) [43].

### 3.8. Electrochemical Performance

To probe the enriched mechanism of the photocatalytic H<sub>2</sub> production, the excitation and transfer of photogenerated charge carriers of the as-synthesized products were studied. The photocurrent-time (PI) as well as the electrochemical impedance spectroscopy (EIS) were employed. The acquired PI profiles are displayed in Figure 8a, which portrays the periodic on-off photocurrent response of all the prepared products under visible light illumination.

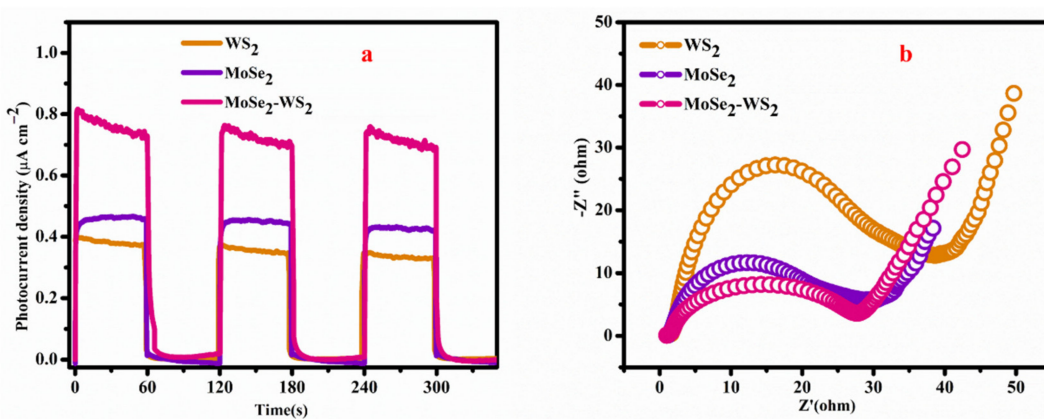


**Figure 8.** (a) Photocurrent response and (b) EIS spectra of WS<sub>2</sub>, MoSe<sub>2</sub> and MoSe<sub>2</sub>-WS<sub>2</sub> nanostructure.

Identically, the photocurrent response of MoSe<sub>2</sub>-WS<sub>2</sub> is higher than that of bare WS<sub>2</sub>, which is consistent with the photocatalytic activity. Measurements carried out in 0.5 mol L<sup>-1</sup> Na<sub>2</sub>SO<sub>4</sub> solution show a photocurrent density of 0.75 μA cm<sup>-2</sup> for the MoSe<sub>2</sub>-WS<sub>2</sub> heterostructure against 0.38 μA cm<sup>-2</sup> for bulk WS<sub>2</sub>. This result demonstrated that the MoSe<sub>2</sub>-WS<sub>2</sub> nanocomposite has a strong ability in transferring and generating the photo-excited charge carrier under the visible light illumination. On the other hand, recombination process and charge transfer of photo-induced electrons as well as holes can be displayed via EIS (Figure 8b). Compared with that of bare MoSe<sub>2</sub> and WS<sub>2</sub> materials, the Nyquist plot evidences clearly a depressed semicircle for MoSe<sub>2</sub>-WS<sub>2</sub>, which designates a fast charge-

carrier transfer rate in the MoSe<sub>2</sub>-WS<sub>2</sub>. Hence, it stipulates that the effective transfer of photo-induced electrons among MoSe<sub>2</sub> and WS<sub>2</sub> enables the electron–hole separation.

### 3.9. Proposed Photocatalytic H<sub>2</sub> Mechanism

In pursuance with the results discussed above, a mechanism for water reduction by the use of MoSe<sub>2</sub>-WS<sub>2</sub> nanostructure-based catalyst is proposed as illustrated by the scheme in Figure 9. The electron–hole pairs are usually generated on MoSe<sub>2</sub>-WS<sub>2</sub> under the visible light illumination. In the development of visible-light-driven devices, the nanostructured MoSe<sub>2</sub>-WS<sub>2</sub> composite is a so-called Z-scheme photocatalyst [44–47]. In this system, electrons are excited from the valence band (VB) to the conduction band (CB) of WS<sub>2</sub> upon visible light illumination, then transferred to VB of MoSe<sub>2</sub> and finally reach to CB of MoSe<sub>2</sub> during generation of H<sub>2</sub>. The photocatalytic H<sub>2</sub> mechanism has been described as follows: in the H<sub>2</sub> evolution setup, the photoreduction of proton by CB electrons as:



and the oxidation of an electron donor (D) by VB holes yields an electron acceptor (A) as:

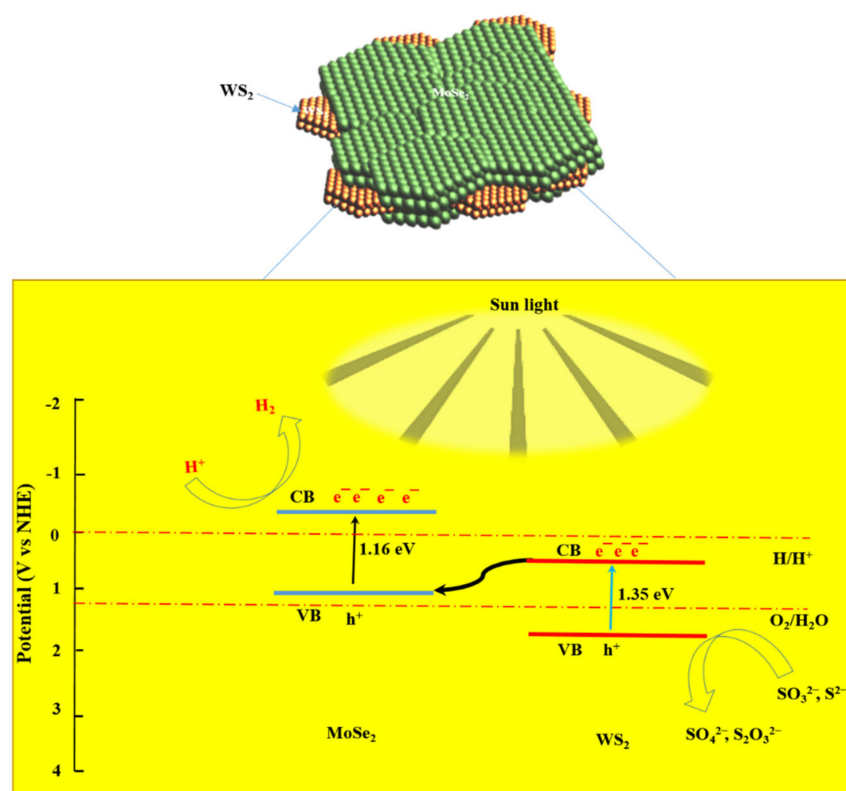


**Figure 9.** Scheme of the photocatalytic mechanism of MoSe<sub>2</sub>-WS<sub>2</sub> nanostructure under light irradiation.

Thus, the water-splitting reaction occurs when a cycle of D and A redox pairs is achieved. Meanwhile, the photogenerated holes on the VB of WS<sub>2</sub> can reduce the scavengers, which considerably decrease the recombination process of electron–hole pairs and lead to improved stability of the MoSe<sub>2</sub>-WS<sub>2</sub> nanostructure and the enhancement of hydrogen production rate. Consequently, the photocatalytic H<sub>2</sub> evolution activity is promoted for WS<sub>2</sub> modified with few MoSe<sub>2</sub> monolayers, which promotes a significant increase of photogenerated charge–hole separation efficiency [48].

#### 4. Conclusions

In summary, we have investigated the structural, vibrational and electronic characteristics of the van der Waals interrelated MoSe<sub>2</sub>-WS<sub>2</sub> nanostructure used as photocatalysts for H<sub>2</sub> production. We found that:

- (1) A cost-effective and simple chemical methodology was handled to fabricate the MoSe<sub>2</sub>-WS<sub>2</sub> nanostructure using an easy one-step hydrothermal process without high-temperature annealing;
- (2) The MoSe<sub>2</sub>-WS<sub>2</sub> nanocomposite has a high specific surface area of 132.79 m<sup>2</sup> g<sup>-1</sup> and a pore size of 10.6 nm, which are values favorable for an efficient photocatalytic activity. For the MoSe<sub>2</sub>-WS<sub>2</sub> heterostructure, in which WS<sub>2</sub> is the core of the sample (bulk) and MoSe<sub>2</sub> is formed by a few nanosheets covering the bulk, the evaluated optical bandgap is 1.24 eV;
- (3) The use of MoSe<sub>2</sub> and WS<sub>2</sub> sheets with similar lattice parameters allows the fabrication of heterostructure without matching restriction;
- (4) The coupling of MoSe<sub>2</sub> with WS<sub>2</sub> led to a considerably enhanced surface area and higher photoinduced charge separation. It results a remarkably improved photocatalytic H<sub>2</sub> production, which was observed by photocurrent measurements and EIS studies;
- (5) Therefore, the resultant MoSe<sub>2</sub>-WS<sub>2</sub> is a capable photocatalyst for the H<sub>2</sub> energy applications. Under LED light irradiation, the MoSe<sub>2</sub>-WS<sub>2</sub> nanostructure demonstrated enhanced photocatalytic hydrogen evolution, which is approximately 3- and 10-times higher compare to bare MoSe<sub>2</sub> and WS<sub>2</sub>. MoSe<sub>2</sub>-WS<sub>2</sub> nanocomposite exhibits a high PHE rate of 1600 μmol g<sup>-1</sup> h<sup>-1</sup>;
- (6) The photocatalytic activity of the MoSe<sub>2</sub>-WS<sub>2</sub> nanostructure can be explained by Z-scheme carrier transfer pathways, which favor the production of reactive species;
- (7) The MoSe<sub>2</sub>/WS<sub>2</sub> heterostructure displayed excellent electrocatalytic hydrogen evolution behavior. The demonstrated hydrogen evolution reaction performance attests to the capability of this nanohybrid to replace the high-cost and scarce Pt and will spark hybrid-based research toward the various future energy sectors. The edges of MoSe<sub>2</sub> and WS<sub>2</sub> present an ideal hydrogen-binding energy, which makes them promising to replace the Pt-based electrocatalysts for hydrogen generation. In addition, the MoSe<sub>2</sub>/WS<sub>2</sub> heterostructure could be a new cost-effective electrode replacing carbon supported Pt and Pt/Ru electrodes in fuel cells.

**Author Contributions:** Conceptualization, methodology, A.N.R.; investigation, D.K.G. and A.N.R.; data curation, T.P., D.K.G., S.V.P.V., and A.N.R.; writing—review and editing, C.M.J.; writing—original draft preparation, supervision, funding acquisition, T.P. and S.V.P.V. All authors have read and agreed to the published version of the manuscript.

**Funding:** This research was funded by the National Research Foundation of Korea (NRF), grant number 2020R1A2B5B01002744.

**Institutional Review Board Statement:** Not applicable.

**Informed Consent Statement:** Not applicable.

**Data Availability Statement:** Data is contained within the article.

**Conflicts of Interest:** The authors declare no conflict of interest.

#### References

1. Peng, W.; Li, Y.; Hang, F.; Zhang, G.; Fan, X. Roles of two-dimensional transition metal dichalcogenides as cocatalysts in photocatalytic hydrogen evolution and environmental remediation. *Ind. Eng. Chem. Res.* **2017**, *56*, 4611–4626. [[CrossRef](#)]
2. Wang, F.; Shifa, T.A.; Zhan, X.; Huang, Y.; Liu, K.; Cheng, Z.; Jiang, C.; He, J. Recent advances in transition-metal dichalcogenide based nanomaterials for water splitting. *Nanoscale* **2015**, *7*, 19764–19788. [[CrossRef](#)] [[PubMed](#)]
3. Voiry, D.; Yang, J.; Chhowalla, M. Recent strategies for improving the catalytic activity of 2D TMD nanosheets toward the hydrogen evolution reaction. *Adv. Mater.* **2016**, *28*, 6197–6206. [[CrossRef](#)] [[PubMed](#)]



4. Mishra, A.K.; Lakshmi, K.V.; Huang, L. Eco-friendly synthesis of metal dichalcogenides nanosheets and their environmental remediation potential driven by visible light. *Sci. Rep.* **2015**, *5*, 15718. [[CrossRef](#)] [[PubMed](#)]
5. Gopannagari, M.; Kumar, D.P.; Reddy, D.A.; Hong, S.; Song, M.I.; Kim, T.K. In situ preparation of few-layered WS<sub>2</sub> nanosheets and exfoliation into bilayers on CdS nanorods for ultrafast charge carrier migrations toward enhanced photocatalytic hydrogen production. *J. Catalys.* **2017**, *351*, 153–160. [[CrossRef](#)]
6. Shanker, G.S.; Biswas, A.; Ogale, S. 2D materials and their heterostructures for photocatalytic water splitting and conversion of CO<sub>2</sub> to value chemicals and fuels. *J. Phys. Energy* **2021**, *3*, 022003. [[CrossRef](#)]
7. Ghatak, K.; Kang, K.N.; Yang, E.; Datta, D. Controlled edge dependent stacking of WS<sub>2</sub>-WS<sub>2</sub> homo- and WS<sub>2</sub>-WSe<sub>2</sub> heterostructures: A computational study. *Sci. Rep.* **2020**, *10*, 1648. [[CrossRef](#)]
8. Thiehm, Z.; Shakoob, A.; Altahtamouni, T. Recent advances in WS<sub>2</sub> and its based heterostructures for water-splitting applications. *Catalysts* **2021**, *11*, 1283. [[CrossRef](#)]
9. Wu, Y.; Liu, Z.; Li, Y.; Chen, J.; Zhu, X.; Na, P. Construction of 2D-2D TiO<sub>2</sub> nanosheet/layered WS<sub>2</sub> heterojunctions with enhanced visible-light-responsive photocatalytic activity. *Chin. J. Catalys.* **2019**, *40*, 60–69. [[CrossRef](#)]
10. Wei, Z.; Huang, W.; Xu, L.; Hu, W.; Peng, P.; Huang, G. Dual functions of 2D WS<sub>2</sub> and MoS<sub>2</sub>-WS<sub>2</sub> monolayers coupled with a Ag<sub>3</sub>PO<sub>4</sub> photocatalyst. *Semicond. Sci. Technol.* **2016**, *31*, 9. [[CrossRef](#)]
11. Jeevanandham, G.; VEDIAPPAN, K.; Allothman, Z.A.; Altalhi, T.; Sundramoorthy, A.K. Fabrication of 2D-MoSe<sub>2</sub> incorporated NiO Nanorods modified electrode for selective detection of glucose in serum samples. *Sci. Rep.* **2021**, *11*, 13266. [[CrossRef](#)] [[PubMed](#)]
12. Zhou, Y.; Zhu, Y.; Chen, X.; Dong, B.; Li, Q.; Chai, Y. Carbon-based transition metal sulfides/selenides nanostructures for electrocatalytic water splitting. *J. Alloy. Compd.* **2021**, *852*, 156810. [[CrossRef](#)]
13. Qi, S.; Liu, X.; Ma, N.; Xu, H. Construction and photocatalytic properties of WS<sub>2</sub>/MoS<sub>2</sub>/BiOCl heterojunction. *Chem. Phys. Lett.* **2021**, *763*, 138203. [[CrossRef](#)]
14. Ho, W.; Yu, J.C.; Lin, J.; Yu, J.; Li, P. Preparation and photocatalytic behavior of MoS<sub>2</sub> and WS<sub>2</sub> nanocluster sensitized TiO<sub>2</sub>. *Langmuir* **2004**, *20*, 5865–5869. [[CrossRef](#)]
15. Tan, C.; Zhang, H. Two-dimensional transition metal dichalcogenide nanosheet-based composites. *Chem. Soc. Rev.* **2015**, *44*, 2713–2731. [[CrossRef](#)]
16. Lu, Q.; Yu, Y.; Ma, Q.; Chen, B.; Zhang, H. 2D transition-metal dichalcogenide-nanosheet-based composites for photocatalytic and electrocatalytic hydrogen evolution reactions. *Adv. Mater.* **2016**, *28*, 1917–1933. [[CrossRef](#)]
17. Amin, B.; Kaloni, T.P.; Schreckenbach, G.; Freund, M.S. Materials properties of out-of-plane heterostructures of MoS<sub>2</sub>-WSe<sub>2</sub> and WS<sub>2</sub>-MoSe<sub>2</sub>. *Appl. Phys. Lett.* **2016**, *108*, 063105. [[CrossRef](#)]
18. Ruiz-Tijerina, D.A.; Fal'ko, V.I. Interlayer hybridization and moiré superlattice minibands for electrons and excitons in heterobilayers of transition-metal dichalcogenides. *Phys. Rev. B* **2019**, *99*, 125424. [[CrossRef](#)]
19. Jin, C.; Ma, E.Y.; Karni, O.; Regan, E.C.; Wang, F.; Heinz, T.F. Ultrafast dynamics in van der Waals heterostructures. *Nat. Technol.* **2018**, *13*, 994–1003.
20. Kozawa, D.; Carvalho, A.; Verzhbitskiy, I.; Giustiniano, F.; Miyauchi, Y.; Mouri, S.; Castro Neto, A.H.; Matsuda, K.; Eda, G. Evidence for fast interlayer energy transfer in MoSe<sub>2</sub>/WS<sub>2</sub> heterostructures. *Nano Lett.* **2016**, *16*, 4087–4093. [[CrossRef](#)]
21. Meng, Y.; Wang, T.; Jin, C.; Li, Z.; Miao, S.; Lian, Z.; Taniguchi, T.; Watanabe, K.; Song, F.; Shi, S.F. Electrical switching between exciton dissociation to exciton funneling in MoSe<sub>2</sub>/WS<sub>2</sub> heterostructure. *Nat. Commun.* **2020**, *11*, 2640. [[CrossRef](#)] [[PubMed](#)]
22. Amin, B.; Kaloni, T.P.; Schwingenschlögl, U. Strain engineering of WS<sub>2</sub>, WSe<sub>2</sub>, and WTe<sub>2</sub>. *RSC Adv.* **2014**, *4*, 34561–34565. [[CrossRef](#)]
23. Ceballos, F.; Ju, M.G.; Lane, S.D.; Zeng, X.C.; Zhao, H. Highly efficient and anomalous charge transfer in van der Waals trilayer semiconductors. *Nano Lett.* **2017**, *17*, 1623–1628. [[CrossRef](#)] [[PubMed](#)]
24. Wu, Z.; Ouyan, M.; Wang, D. Construction of WS<sub>2</sub>/MoSe<sub>2</sub> heterojunction for efficient photoelectrocatalytic hydrogen evolution. *Mater. Sci. Semicond. Process* **2020**, *107*, 104822. [[CrossRef](#)]
25. Jaramillo, T.F.; Jørgensen, K.P.; Bonde, J.; Nielsen, J.H.; Horch, S.; Chorkendorff, I. Identification of active edge sites for electrochemical H<sub>2</sub> evolution from MoS<sub>2</sub> nanocatalysts. *Science* **2007**, *317*, 100–102. [[CrossRef](#)]
26. Kang, J.; Tongay, S.; Zhou, J.; Li, J.; Wu, J. Band offsets and heterostructures of two-dimensional semiconductors. *Appl. Phys. Lett.* **2013**, *102*, 012111. [[CrossRef](#)]
27. Vikraman, D.; Hussain, S.; Truong, L.; Karuppasamy, K.; Kim, H.J.; Maiyalagan, T.; Chun, S.H.; Jung, J.; Kim, H.S. Fabrication of MoS<sub>2</sub>/WSe<sub>2</sub> heterostructures as electrocatalyst for enhanced hydrogen evolution reaction. *Appl. Surf. Sci.* **2019**, *480*, 611–620. [[CrossRef](#)]
28. Vikraman, D.; Hussain, S.; Patil, S.A.; Truong, L.; Arbab, A.A.; Jeong, S.H.; Chun, S.H.; Jung, J.; Kim, H.-S. Engineering MoSe<sub>2</sub>/WS<sub>2</sub> hybrids to replace the scarce platinum electrode for hydrogen evolution reactions and dye-sensitized solar cells. *ACS Appl. Mater. Interfaces* **2021**, *123*, 5061–5072. [[CrossRef](#)]
29. Yuan, Z.; Jiang, Q.; Feng, C.; Chen, X.; Guo, Z. Synthesis and performance of tungsten disulfide/carbon (WS<sub>2</sub>/C) composite as anode material. *J. Electron. Mater.* **2018**, *47*, 251–260. [[CrossRef](#)]
30. Xiong, M.; Qian, J.; Yang, K.; Chen, Z.; Mei, T.; Wang, J.; Li, J.; Yu, L.; Wang, X. Efficient polysulfide anchor: Brain coral-like WS<sub>2</sub> nanosheets. *J. Mater. Sci.* **2020**, *55*, 12031–12040. [[CrossRef](#)]
31. Zhao, Y.; Liu, J.; Zhang, X.; Wang, C.; Zhao, X.; Li, J.; Jin, H. Convenient synthesis of WS<sub>2</sub>-MoS<sub>2</sub> heterostructures with enhanced photocatalytic performance. *J. Phys. Chem. C* **2019**, *123*, 27363–27368. [[CrossRef](#)]

32. Eftekhari, A. Molybdenum diselenide (MoSe<sub>2</sub>) for energy storage, catalysis, and optoelectronics. *Appl. Mater. Today* **2017**, *8*, 1–17. [[CrossRef](#)]
33. Peng, K.; Wang, H.; Li, X.; Wang, J.; Cai, Z.; Su, L.; Fan, X. Emerging WS<sub>2</sub>/montmorillonite composite nanosheets as an efficient hydrophilic photocatalyst for aqueous phase reactions. *Sci. Rep.* **2019**, *9*, 16325. [[CrossRef](#)] [[PubMed](#)]
34. Vaziri, H.S.; Shokuhfar, A.; Afghah, S.S.S. Synthesis of WS<sub>2</sub>/CNT hybrid nanoparticles for fabrication of hybrid aluminum matrix nanocomposite. *Mater. Res. Express* **2020**, *7*, 025034. [[CrossRef](#)]
35. Li, X.; Peng, K. MoSe<sub>2</sub>/montmorillonite composite nanosheets: Hydrothermal synthesis, structural characteristics, and enhanced photocatalytic activity. *Minerals* **2018**, *8*, 268. [[CrossRef](#)]
36. Zeng, P.; Ji, X.; Su, Z.; Zhang, S. WS<sub>2</sub>/g-C<sub>3</sub>N<sub>4</sub> composite as an efficient heterojunction photocatalyst for biocatalyzed artificial photosynthesis. *RSC Adv.* **2018**, *8*, 20557–20567. [[CrossRef](#)]
37. Gusakova, J.; Wang, X.; Shiau, L.L.; Krivosheeva, A.; Shaposhnikov, V.; Borisenko, V.; Gusakov, V.; Tay, B.K. Electronic properties of bulk and monolayer TMDs: Theoretical study within DFT framework (GVJ-2e method). *Phys. Status Solidi A* **2017**, *214*, 1700218. [[CrossRef](#)]
38. Rusu, D.I.; Rusu, G.G.; Luca, D. Structural characteristics and optical properties of thermally oxidized zinc films. *Acta Phys. Polonica A* **2011**, *119*, 850–856. [[CrossRef](#)]
39. Tauc, J. *Optical Properties of Solids*; Abeles, F., Ed.; North-Holland: Amsterdam, The Netherlands, 1972.
40. Zanatta, A.R. Revisiting the optical bandgap of semiconductors and the proposal of a unified methodology to its determination. *Sci. Rep.* **2019**, *9*, 11225. [[CrossRef](#)]
41. Yoffe, A.D. Low-dimensional systems: Quantum size effects and electronic properties of semiconductor microcrystallites (zero-dimensional systems) and some quasi-two-dimensional systems. *Adv. Phys.* **1993**, *42*, 173–266. [[CrossRef](#)]
42. Wang, Q.H.; Kalantar-Zadeh, K.; Kis, A.; Coleman, J.N.; Srano, M.S. Electronics and optoelectronics of two-dimensional transition metal dichalcogenides. *Nat. Nanotechnol.* **2012**, *7*, 699–712. [[CrossRef](#)] [[PubMed](#)]
43. Ding, Y.; Wang, Y.; Ni, J.; Shi, L.; Shi, S.; Tang, W. First principles study of structural, vibrational and electronic properties of graphene-like MX<sub>2</sub> (M=Mo, Nb, W, Ta; X=S, Se, Te) monolayers. *Phys. B* **2011**, *406*, 2254–2260. [[CrossRef](#)]
44. Police, A.K.R.; Vattikuti, S.V.P.; Mandari, K.K.; Chennaiahgari, M.; Sharma, P.; Vallurid, D.K.; Byon, C. Bismuth oxide cocatalyst and copper oxide sensitizer in Cu<sub>2</sub>O/TiO<sub>2</sub>/Bi<sub>2</sub>O<sub>3</sub> ternary photocatalyst for efficient hydrogen production under solar light irradiation. *Ceram. Int.* **2018**, *44*, 11783–11791. [[CrossRef](#)]
45. Maeda, K. Z-scheme water splitting using two different semiconductor photocatalysts. *ACS Catal.* **2013**, *3*, 1486–1503. [[CrossRef](#)]
46. Wang, G.; Chang, J.; Tang, W.; Xie, W.; Ang, Y.S. 2D materials and heterostructures for photocatalytic water-splitting: A theoretical perspective. *J. Phys. D Appl. Phys.* **2022**, *5*, 293002. [[CrossRef](#)]
47. Fu, C.; Wang, G.; Huang, Y.; Chen, Y.; Yuan, H.; Ang, Y.S.; Chen, H. Two-dimensional CdS/SnS<sub>2</sub> heterostructure: A highly efficient direct Z-scheme water splitting photocatalyst. *Phys. Chem. Chem. Phys.* **2022**, *24*, 3826–3833. [[CrossRef](#)] [[PubMed](#)]
48. Cui, L.; Xiang Ding, X.; Wang, Y.; Shi, H.; Huang, L.; Zuo, Y.; Kang, S. Facile preparation of Z-scheme WO<sub>3</sub>/g-C<sub>3</sub>N<sub>4</sub> composite photocatalyst with enhanced photocatalytic performance under visible light. *Appl. Surface Sci.* **2017**, *391*, 202–210. [[CrossRef](#)]